

The effects of rotation on the s-process nucleosynthesis in Asymptotic Giant Branch stars

L. Piersanti

INAF-Osservatorio Astronomico di Collurania, via Maggini snc, 64100, Teramo, Italy

`piersanti@oa-teramo.inaf.it`

S. Cristallo

INAF-Osservatorio Astronomico di Collurania, via Maggini snc, 64100, Teramo, Italy

O. Straniero

INAF-Osservatorio Astronomico di Collurania, via Maggini snc, 64100, Teramo, Italy

October 14, 2018

Received _____; accepted _____

ABSTRACT

In this paper we analyze the effects induced by rotation on low mass Asymptotic Giant Branch stars. We compute two sets of models, $M=2.0 M_{\odot}$ at $[\text{Fe}/\text{H}]=0$ and $M=1.5 M_{\odot}$ at $[\text{Fe}/\text{H}]=-1.7$, respectively, by adopting Main Sequence rotation velocities in the range $0\div 120$ km/s. At high metallicity, we find that the Goldreich-Schubert-Fricke instability, active at the interface between the convective envelope and the rapid rotating core, contaminates the ^{13}C -pocket (the major neutron source) with ^{14}N (the major neutron poison), thus reducing the neutron flux available for the synthesis of heavy elements. As a consequence, the yields of heavy-s elements (Ba, La, Nd, Sm) and, to a less extent, those of light-s elements (Sr, Y, Zr) decrease with increasing rotation velocities up to 60 km/s. However, for larger initial rotation velocities, the production of light-s and, to a less extent, that of heavy-s begins again to increase, due to mixing induced by meridional circulations. At low metallicity, the effects of meridional circulations are important even at rather low rotation velocity. The combined effect of Goldreich-Schubert-Fricke instability and meridional circulations determines an increase of light-s and, to a less extent, heavy-s elements, while lead is strongly reduced. For both metallicities, the rotation-induced instabilities active during the interpulse phase reduce the neutrons-to-seeds ratio, so that the spectroscopic indexes $[\text{hs}/\text{ls}]$ and $[\text{Pb}/\text{hs}]$ decrease by increasing the initial rotation velocity. Our analysis suggests that rotation could explain the spread in the s-process indexes, as observed in s-process enriched stars at different metallicities.

Subject headings: Stars: rotation — Stars: AGB and post-AGB — Nuclear reactions, nucleosynthesis, abundances

1. Introduction

Rotation modifies the physical structure and the chemical composition of a star, essentially because of the lifting due to the centrifugal force and of the mixing induced by dynamical and secular instabilities. The lifting effects on AGB stars have been firstly studied by Dominguez et al. (1996), who showed that it causes a delay of the second dredge up in intermediate mass stars and, in turn, allows the formation of CO cores very close to the Chandrasekhar limit for a non-rotating degenerate stellar structure. More recently, models of low-mass AGB stars including the effects of rotation have been discussed by several authors (Langer et al. 1999; Herwig et al. 2003; Siess et al. 2004). Due to the relatively small initial angular momentum of the majority of low mass stars, lifting effects are generally negligible in single stars with mass lower than $3 M_{\odot}$. Nonetheless, mixing induced by rotation may have important consequences on the nucleosynthesis. Indeed, low-mass AGB stars play a fundamental role in the chemical evolution of their host galaxy, being the main producers of about half of the elements heavier than iron. They also contribute to the synthesis of some light elements, like carbon or fluorine. During the late part of the AGB phase, these stars undergo recursive thermal pulses, *i.e.* thermonuclear runaways of the He-burning layer (Thermally Pulsing Asymptotic Giants Branch stars, TP-AGB stars). If the envelope mass exceeds a critical value, the thermal pulse is followed by a third dredge up episode (TDU), *i.e.* a deep penetration of the convective envelope into the H-exhausted region (for a review see Iben & Renzini 1983 and Straniero et al. 2006). As a consequence, the products of the internal nucleosynthesis appear at the surface. In addition, when the convective envelope recedes, a thin zone characterized by a variable profile of hydrogen is left on the top of the H-exhausted core. During the time that elapses between two successive thermal pulses (interpulse period), this zone contracts and heats up, until ^{13}C and ^{14}N are produced as a consequence of an incomplete CN cycle. The resulting ^{13}C enriched zone is often called the ^{13}C pocket. Just above this layer, a ^{14}N pocket forms. As firstly shown by Straniero et al. (1995) (see also Gallino et al. 1998), when the temperature approaches ~ 90 MK, the $^{13}\text{C}(\alpha, n)^{16}\text{O}$ reaction provides the neutron flux needed to

activate an efficient s-process nucleosynthesis. Gallino et al. (1998) demonstrate that about $10^{-5} M_{\odot}$ of ^{13}C are required to reproduce the heavy element enhancements commonly observed in evolved AGB and post-AGB stars (Lambert et al. 1995; Abia et al. 2001, 2002; Reyniers et al. 2004). As a matter of fact, the theoretical tools commonly used to model AGB stars do not provide a precise quantitative description of the H abundance left by the TDU in the transition zone between the fully convective envelope and the radiative core. In turn, the extension of the ^{13}C pocket is not very well constrained on the base of first principles. This problem has been largely discussed in the community of stellar modelers. One of the main open-questions concerns the physical process(es) that determines such a H profile. Herwig et al. (1997) firstly supposed that the driving process is the convective overshoot. Then, to model such an overshoot, they adopted an exponential decay of the diffusion coefficient at the convective boundaries. Becker & Iben (1980), Castellani et al. (1990) and Mowlavi (1999) noted that the inner border of the convective envelope becomes dynamically unstable when it penetrates an He-rich (or a H-exhausted) region, as it happens during a TDU episode. In our previous works (for details see Straniero et al. 2006), in order to handle such an instability, we followed an approach similar to the one introduced by Herwig et al. (1997), by assuming an exponential decay of the average convective velocity at the inner border of the convective envelope. The calibration of the free parameter, namely the strength of the exponential decay, has been discussed in Cristallo et al. (2009). Langer et al. (1999) investigated the possibility that rotation-induced mixing, rather than convective instabilities, may generate a variable H profile on the top of the H-exhausted core. Note that the mixing of protons should occur within the relatively short period of time elapsing between the occurrence of the TDU and the restart of the H-burning, when the ^{13}C pocket develops. More recent studies have shown that a Goldreich-Schubert-Fricke (hereinafter GSF) instability actually arises during this period of time, but the resulting amount of ^{13}C is about one order of magnitude smaller than that required to reproduce the observed overabundances of heavy elements (Herwig et al. 2003; Siess et al. 2004). Although these studies cast doubts on the possibility that rotation alone could

produce a sizeable ^{13}C pocket, nonetheless mixing induced by rotation may still play a significant role in the s-process nucleosynthesis in low mass AGB stars. Independently on the processes that determine the variable H pattern after a TDU episode¹, rotation-induced mixing may spread out the ^{13}C pocket. In that case, owing to the contamination of the ^{13}C -rich zone with a significant amount of ^{14}N , most of the neutrons released by the $^{13}\text{C}(\alpha, n)^{16}\text{O}$ will be captured by the ^{14}N , thus reducing the s-process production of heavy elements (Siess et al. 2004). In addition, since the ^{13}C spreads over a larger zone, the average value of the neutrons-to-seeds ratio is expected to decrease. As a result, the abundance of light-s, namely Sr, Y, Zr (hereinafter ls), heavy-s, namely Ba, La, Nd, Sm (hereinafter hs) and lead² could be strongly modified.

The purpose of this paper is to investigate the effects of the rotation-induced instabilities on the nucleosynthesis occurring in low-mass TP-AGB stars. More specifically, we add rotation-induced mixing to the other mixing already considered in our previous works, those due to convection in particular. As in our previous works, the leading process determining the formation of the ^{13}C pocket is the dynamical instability affecting the inner border of the convective envelope during a TDU episode. Then, we allow rotation to possibly modify the physical conditions, such as temperature and density, as well as the chemical stratification of the layers where neutrons are released and the s process takes place.

¹For completeness, we recall that in addition to convection and rotation, other physical processes have been considered as possible origin of the ^{13}C pocket (*e.g.* *Denissenkov & Tout 2003*)

²The definition of ls and hs may vary from author to author. Usually, these quantities identify elements with a magic isotope, *i.e.* a nucleus having a particularly stable nuclear structure.

2. Algorithm and input physics

The large majority of stars belonging to the Galactic Disk with mass $M < 3M_{\odot}$ show rotation velocities < 80 km/s, with mean values varying from author to author (see, *e.g.*, Groot et al. 1996; de Medeiros & Mayor 1999; Holmberg et al. 2007; Ammler-von Eiff & Reiners 2012). Since more compact stars are expected at low metallicities, Halo stars in the same range of mass were, possibly, faster rotators. We have computed two sets of stellar evolutionary models for two different chemical compositions. The first set has solar-scaled composition with $Y=0.269$ and $[\text{Fe}/\text{H}]=0$ (corresponding to $Z=1.4\times 10^{-2}$). The second set has $Y=0.245$, $[\text{Fe}/\text{H}]=-1.7$ and $[\alpha/\text{Fe}]=0.5$ (corresponding to $Z=7\times 10^{-4}$). The initial masses are $M=2.0 M_{\odot}$ for the high metallicity set and $M=1.5 M_{\odot}$ for the low metallicity one. Each sequence starts with a contracting pre-Main-Sequence fully-homogeneous model and we follow its evolution up to the AGB tip. At the Zero Age Main Sequence, models are assumed to uniformly rotate, with initial rotation velocities $v_{rot}^{ini}=0, 10, 30, 60$ or 120 km/s for both the metallicity sets. The initial angular velocity ω_0 and total angular momentum J_0 of each model are listed in Table 1.

All the models have been computed with the evolutionary code described in Straniero et al. (2006), modified to account for rotation. The adopted nuclear network includes about 500 isotopes (from ^1H to ^{209}Bi), coupled by more than 1000 reactions. The physical inputs, such as the Equation of State, the radiative and the conductive opacity, the strong and the weak reaction rates, are the same as in Cristallo et al. (2009). The solar composition has been taken from Lodders (2003). Accordingly, the value of mixing length parameter, namely $\alpha=2.1$, has been derived by computing a standard solar model as described in Piersanti et al. (2007).

The effects of rotation on the structural equations have been accounted for according to the procedure described by Endal & Sofia (1976). In particular, for the gravitational plus rotational potential we adopt the approximation by Kippenhahn & Thomas (1970), *i.e.* the radial component of the centrifugal force is averaged over a sphere (see Piersanti et al. 2003, 2010;

Tornambé & Piersanti 2013). In addition, a corrective term for the radiative temperature gradient is included in the energy transport equation (Endal & Sofia 1976). In order to compute realistic models one has also to include a description of the angular momentum transport as determined by both convection and rotation-induced instabilities. In addition, the angular momentum profile within a structure as a function of time determines whether or not macroscopic mass motions occur, thus also affecting the chemical stratification.

The treatment of angular momentum transport is currently one of the main problems of evolutionary models computed with 1D hydrostatic codes including rotation. In fact, the efficiency of rotation-induced instabilities relies on phenomenological theories so that they have to be regarded as order-of-magnitude estimates. Such an approach inevitably implies the introduction of free parameters, which require an appropriate calibration³. Observations can be used to constrain the adopted efficiency even if, up to now, direct measurements of the internal angular momentum are available only for a small sample of low mass Main Sequence (MS) and Red Giant (RG) stars. The data obtained by KEPLER for a sample of RG stars with masses around $1.3 M_{\odot}$ and metallicity close to solar show that the ratio between the angular velocity of the He core and of the surface is about 5-10, while theoretical models including the effects of rotation predict a definitely larger value (up to 1000; see for instance Eggenberger et al. 2012; Marques et al. 2013). Moreover, the experimental determination of the rotation velocity for a sample of DA White Dwarfs (WDs) provides a value lower than 10 km/s (Berger et al. 2005), while the extant theoretical models of low mass AGB stars predict rapidly spinning CO cores. Such an evidence clearly suggest that in the current modelling of the evolution of rotating stars either the transport of angular momentum is underestimated by at least two orders of magnitude (Marques et al. 2013) or some additional mechanisms responsible for an efficient extraction of angular momentum from

³Note that this approach is similar to the one commonly used to calibrate the efficiency of convective transport, as it is done, for example, in the case of the mixing length theory.

the core are currently neglected. Magnetic torque could be a possible solution (Spruit 2002; Suijs et al. 2008), although it is not clear if the dynamo process could be active also in the radiative envelope of MS stars (see the discussion in Langer 2012). Nonetheless, the narrow extension of the solar tachocline suggests the presence in the radiative inner zones of a fossil magnetic field (Gough & McIntyre 1998), which could brake the solar core by magnetic torque (Spruit 1998, 2002). However, Denissenkov & Pinsonneault (2007) argued that a solar models including only this mechanism would result in a rapidly rotating core, in contradiction with helioseismic data. They concluded "that the Tayler-Spruit mechanism may be important for envelope angular momentum transport but that some other process must be responsible for efficient spin-down of stellar cores". Alternatively, gravity waves could extract angular momentum from the inner zones of a star determining the observed features (see Zahn et al. 1997, and references therein). Other constraints on the angular momentum transport and, hence, on the corresponding mixing efficiency can be put basing on chemical abundances observed in stars. The solar lithium abundance seems to indicate that the mixing related to rotation-induced instabilities has an efficiency smaller than the one for the transport of angular momentum (Pinsonneault et al. 1989). Moreover, the observed nitrogen surface enrichment in massive stars (Przybilla et al. 2010) is considered an indication that the damping effect of mean molecular weight (μ) gradient on meridional circulations is smaller than the current estimates (Heger et al. 2000; Yoon et al. 2006; Brott et al. 2011). Summarizing, the issue of the actual efficiency of the angular momentum transport in stars is, so far, an open problem.

In this paper we adopt a common procedure based on diffusion algorithms to describe the angular momentum transport and the mixing of the chemical species induced by rotation. Following Pinsonneault et al. (1989) (see also Heger et al. 2000, Yoon et al. 2006 and Brott et al. 2011) we introduce some free parameters to account for the many uncertainties due to rotation instabilities and to additional phenomena, such has the magnetic braking, not explicitly included.

Following Endal & Sofia (1978), we adopt a non-linear diffusion equation to describe the

transport of angular momentum:

$$\left(\frac{\partial\omega}{\partial t}\right) = \frac{1}{i} \frac{\partial}{\partial m} \left[(4\pi r^2 \rho)^2 i D_J \left(\frac{\partial\omega}{\partial m}\right) \right] \quad (1)$$

where i is the specific moment of inertia, ω the angular velocity (in rad/s), ρ the density (in $\text{g} \cdot \text{cm}^{-3}$) and r and m the radius and mass coordinate, respectively. D_J is the total diffusion coefficient for angular momentum transport defined as the sum of the diffusion coefficients related to convection and both secular and dynamical rotation-induced instabilities:

$$D_J = D_{conv} + f_\omega \times (D_{ES} + D_{GSF} + D_{SS} + D_{DS} + D_{SH}) \quad (2)$$

where D_{ES} , D_{GSF} , D_{SS} , D_{DS} , D_{SH} are the diffusion coefficients related to Eddington-Sweet, Goldreich-Schubert-Fricke, Secular Shear, Dynamical Shear and Solberg-Höiland instabilities, respectively. At the center ($m = 0$) and at the surface ($m = M$) reflecting conditions are assumed. Such a formulation guarantees the conservation of the total angular momentum and enforces rigid rotation in the zones where the diffusion timescale is shorter than the ones for a structural change of the star. The parameter f_ω accounts for possible uncertainties affecting the angular momentum transport.

The diffusion coefficient for convection is computed according to the mixing length theory (Cox 1968). The other diffusion coefficients are given by the product of a scale length (l) and a characteristic circulation velocity v . According to Endal & Sofia (1978), the scale length is defined as:

$$l = \min \left[\Delta r, \left| \frac{\partial \ln v}{\partial r} \right|^{-1} \right] \quad (3)$$

where Δr is the extension of the unstable zone.

Variations of the chemical species, as due to convection and rotation-induced mixing, is also described by means of a nonlinear diffusion equation:

$$\left(\frac{\partial X_k}{\partial t}\right) = \frac{\partial}{\partial m} \left[(4\pi r^2 \rho)^2 D_C \left(\frac{\partial X_k}{\partial m}\right) \right] \quad (4)$$

where X_k represent the mass fraction of the k chemical species. In order to take into account the variations of ω and μ into the diffusion coefficients, Eqs. (1) and (4) should be coupled.

The total diffusion coefficient in Eq. (4) is:

$$D_C = D_{conv} + f_\omega \times f_c \times (D_{ES} + D_{GSF} + D_{SS} + D_{DS} + D_{SH}) \quad (5)$$

where f_c is intended to reduce the matter circulation with respect to the angular momentum transport, and should be ≤ 1 . Pinsonneault et al. (1989) obtained $f_c = 0.046$ by fitting the solar lithium surface abundance. The physical motivation for such a factor was provided by Chaboyer & Zahn (1992), who showed that, under the hypothesis of shellular rotation, horizontal turbulence inhibits vertical mixing whereas angular momentum transport is not affected. As a consequence, in an Eddington-Sweet unstable zone meridional circulations arise, determining an angular momentum transport more efficient than the corresponding mixing of chemical species. According to Chaboyer & Zahn (1992), the ratio of the diffusion efficiency over the turbulent viscosity is $f_c = 1/30$. Such a value has been adopted by many authors (Heger et al. 2000; Yoon & Langer 2004; Heger et al. 2005; Petrovic et al. 2005; Yoon & Langer 2005; Yoon et al. 2006; Suijs et al. 2008), even if a slightly lower f_c has been adopted by Brott et al. (2011) to reproduce the surface abundances of a B-stars sample in the Large Magellanic Cloud obtained by the FLAMES survey ($f_c=0.028$). Note that, in the previous listed works, as well as in the present one, such a parameter has been used to reduce the mixing efficiency of all the rotation-induced instabilities even if, in principle, it should be applied to meridional circulations only.

As it will be shown in the following sections, the rotation instabilities affecting the s-process nucleosynthesis during the AGB evolution of low mass stars are the Eddington-Sweet and the Goldreich-Schubert-Fricke instabilities. The meridional circulations velocity of a mass flow can be derived by estimating the mass flux needed to balance the von Zeipel effect (Kippenhahn 1974) and in chemically homogeneous regions it is given by the following relation:

$$v_{ES} = \frac{\nabla_{ad}}{\delta(\nabla_{ad} - \nabla)} \frac{\omega^2 r^3 L}{(Gm)^2} \left[\frac{2\epsilon r^2}{L} - \frac{2r^2}{m} - \frac{3}{4\pi\rho r} \right] \quad (6)$$

Goldreich & Schubert (1967) and independently Fricke (1968) demonstrated that in radiative chemically-homogeneous zones differential rotation is stable when the specific angular momentum is an increasing function of the radius. By assuming cylindrical symmetry this corresponds to the following conditions:

$$\frac{\partial j}{\partial z} = 0; \quad \frac{\partial j}{\partial w} \geq 0 \quad (7)$$

where w is the distance from the axis of rotation. Such a condition is also sufficient when considering axisymmetric perturbations. James & Kahn (1971) provided an estimate for the large-scale circulation velocity, that in the equatorial plane is given by:

$$v_{GSF} = \frac{2H_T r}{H_j} \left(\frac{2\omega}{r \frac{\partial \omega}{\partial r}} + 1 \right)^{-1} v_{ES} \quad (8)$$

where H_T and H_j are the temperature and specific angular momentum scale height, respectively, and v_{ES} is the Eddington-Sweet circulation velocity. By an inspection to Eqs. (6) and (8), it comes out that the ES circulation dominates in zones where the angular velocity gradient is small, while GSF circulation becomes an important mechanism in zones with a steep μ and ω gradient, as in the case of radiative regions located close to a convective boundary.

As usual, we model the effect of μ -gradient barriers by defining an equivalent μ -current which works against the rotation-induced circulation. The corresponding velocity has been estimated according to Kippenhahn (1974):

$$v_\mu = f_\mu \frac{H_P}{\tau_{th}} \frac{\varphi \nabla_\mu}{\nabla - \nabla_{ad}} \quad (9)$$

where H_P is the pressure scale height, ∇_μ is the mean molecular weight gradient, τ_{th} is the thermal relaxation timescale of a bubble having a different μ with respect to the surrounding and φ is, as usual, $(\partial \ln \rho / \partial \ln \mu)_{P,T}$. According to the previous discussion, the parameter f_μ has been introduced to explore the sensitivity of the obtained results on the adopted formulation for the μ currents.

In the extant literature different values have been adopted for such a parameter: 1.00 (Pinsonneault et al. 1989), 0.05 (Heger et al. 2000), 0.10 (Yoon et al. 2006; Brott et al. 2011). As

noted by Heger et al. (2000), according to the available abundance determinations in massive stars, it is not possible to define the values of both f_c and f_μ univocally, as ”*different combinations might result in similar surface enrichments*”, even if the corresponding angular momentum profiles could be different (see also the discussion in Chieffi & Limongi 2013).

In our standard case we adopt $f_\mu=f_c=f_\omega=1$. In §4 we discuss the effects induced by a variation of these parameters on the s-process nucleosynthesis.

The models computed in the present work does not have a convective envelope during the MS phase, so that we neglect the magnetic braking by stellar winds (Kawaler 1988).

Mass loss rate is computed according to the Reimers’ formula (Reimers 1975), by taking $\eta = 0.4$, except for the AGB phase where we adopt the mass-loss rate described in Straniero et al. (2006). Accordingly, we assume that the matter lost (ΔM) carries away an amount of angular momentum given by:

$$\Delta J = \int_{M-\Delta M}^M j(m)dm \quad (10)$$

where M is the total mass of the star and $j(m)$ is the specific angular momentum.

As recalled in §1, during the TDU a sharp discontinuity in the chemical composition takes place at the convective-radiative boundary, causing the onset of a dynamical instability. In order to handle this instability, Straniero et al. (2006) introduced a transition zone between the fully convective envelope and the radiative core, where the convective velocity exponentially drops from about 10^5 cm/s to zero. The strength of the exponential decaying velocity has been calibrated by Cristallo et al. (2009), who derived a best value of 0.1 pressure scale height. The need for such a transition zone still remains in rotating models, because the velocities of rotation-induced instabilities are 3-4 orders of magnitude smaller than those of convection. In the AGB models here presented, mixing and angular momentum transport in the convective envelope are treated

according to the time-dependent algorithm described in Straniero et al. (2006).

3. Results

3.1. Evolution before the TP-AGB phase

The evolution of angular velocity and angular momentum for the model with $M=2 M_{\odot}$, $[\text{Fe}/\text{H}]=0$ and $v_{rot}^{ini} = 30$ km/s is illustrated in Figure 1. After the exhaustion of the central H, the core contracts and, in turn, spins up. On the contrary, the external layers expand (Red Giant Branch, RGB), so that the angular velocity of the whole convective envelope substantially decreases. Nevertheless, the overall characteristics of the computed evolutionary sequences are very marginally affected by rotation. This is shown in Table 1, where we report as a function of the mass, $[\text{Fe}/\text{H}]$ and v_{rot}^{ini} , the following quantities: MS lifetime (τ_{MS}), mass of the He core at the tip of the RGB phase ($M_{\text{H}}^{\text{TIP}}$), He-burning lifetime ($\tau_{\text{He-burn}}$), stellar age at the beginning of the AGB phase (t_{AGB}), mass of the CO core at t_{AGB} ($M_{\text{CO}}^{\text{AGB}}$), mass of the He core at τ_{AGB} ($M_{\text{H}}^{\text{AGB}}$) and final central C/O ratio. We note that the MS lifetime for the model with $M=2 M_{\odot}$, $[\text{Fe}/\text{H}]=0$ and $v_{rot}^{ini} = 120$ km/s is just 1% longer than the one of the corresponding non-rotating model, while in the low metallicity set this difference becomes 2.5%. This is a consequence of the lifting caused by rotation during the MS. At the RGB tip, when He-burning starts, the He-core mass of the model with $M=2.0 M_{\odot}$, $[\text{Fe}/\text{H}]=0$ and $v_{rot}^{ini}=120$ km/s is only $0.006 M_{\odot}$ larger than that of the corresponding non-rotating model. At low metallicity such a difference is $0.002 M_{\odot}$. However, it is worth noting that the small variation of the He-core mass at the RGB tip determines a slightly larger luminosity during the Horizontal Branch phase. As a consequence, the nuclear energy is released at a larger rate to balance the higher surface radiative losses. Therefore, larger initial rotation velocities imply higher central temperatures and, hence, shorter He-burning lifetimes. In any case, the variation of $\tau_{\text{He-burn}}$ in our models is smaller than 5%. As a result, the central C/O ratio at the end of the core-He burning phase is slightly larger in rotating models. At the

beginning of the AGB phase the physical and chemical structures of the rotating models are slightly different from those of the corresponding non-rotating models. In particular, increasing the initial rotation velocity, the CO core mass grows up to $2 \times 10^{-2} M_{\odot}$ and $1.3 \times 10^{-2} M_{\odot}$ for the $[\text{Fe}/\text{H}]=0$ and $[\text{Fe}/\text{H}]=-1.7$ sets, respectively. Similarly, the mass of the H-exhausted core increases up to $1.5 \times 10^{-2} M_{\odot}$ and $10^{-2} M_{\odot}$, respectively.

3.2. TP-AGB evolution and the ^{13}C pocket: the $[\text{Fe}/\text{H}]=0$ case

The changes caused by rotation on the evolution preceding the TP-AGB phase are small enough that the development of thermal pulses and the subsequent dredge up episodes are substantially unaffected. Several rotation-induced instabilities affecting the s-process nucleosynthesis, but not modifying the overall physical properties of the models, arise during the TP-AGB phase.

In order to describe the effects of angular momentum transport and chemical mixing on the evolution of AGB models we illustrate the formation and evolution of the 2^{nd} ^{13}C pocket, which forms between the 2^{nd} and the 3^{rd} TPs, in $2 M_{\odot}$ and $[\text{Fe}/\text{H}]=0$ models with different initial rotation velocities. In Figure 2 we report the evolution of the borders of the rotation-induced unstable zones relevant for the s-process nucleosynthesis as well as of convective regions during that interpulse period. We also plot the ^{13}C pocket (vertical shaded region⁴). In Figure 3 we plot the mass fractions of selected key isotopes in the top layer of the H-exhausted core, namely ^1H (solid curve), ^{13}C (dotted curve), ^{14}N (short-dashed curve), ^{89}Y (long-dashed curve), ^{139}La (dot-short-dashed curve) and ^{208}Pb (dot-long-dashed curve). The four panels in each column refer to the following epochs:

⁴We define this region as the layer where $X(^{13}\text{C}) > 10^{-3}$.

- $t = 0$, maximum penetration of the convective envelope during the TDU;
- $t = 3.0 \times 10^4$ yr, complete development of the ^{13}C pocket;
- $t = 8.0 \times 10^4$ yr, start of the s-process nucleosynthesis;
- $t = 1.5 \times 10^5$ yr, end of the s-process nucleosynthesis.

The occurrence of the TP drives the formation of a convective shell which fully mixes the He-intershell region (magenta spikes in Figure 2). When the TP quenches and this convective shell disappears, the He-intershell is nearly homogeneous, so that it becomes unstable to meridional circulations (red zone). Later on, when the He-burning shell moves outward, the He-intershell expands, the convective envelope (oblique shaded area) penetrates inward and, then, recedes, leaving a variable H profile. The resulting steep μ -gradient acts as a barrier for meridional circulations. In models with low v_{rot}^{ini} , the ES unstable zone only marginally overlaps to the layer of variable hydrogen profile. In any case, the circulation velocity is rather low. Increasing the initial rotation velocity, v_{ES} increases as well as the extension of the overlapped layer, thus determining an inward mixing of hydrogen (see first row in Figure 3). Note that when the H mass fraction does not exceeds a few 10^{-4} , an incomplete CN cycle takes place, so that the ^{13}C production is favored with respect to the ^{14}N production. As a consequence, the inward mixing induced by meridional circulations will imply more extended ^{13}C pockets (see second row in Figure 3). Since the meridional circulations remain active during the whole interpulse, also the products of the s process will be slowly mixed inward (see third and forth rows in Figure 3).

In addition to the meridional circulations another secular instability takes place after the TDU (blue zone in Figure 2). In Figure 4 we report ω (upper panel) and the specific angular momentum profiles (lower panel) for the model with $v_{rot}^{ini}=60$ km/s. As shown in this Figure, a sharp drop of the angular momentum develops in the transition zone between the fast-rotating core and the

slow-rotating envelope. The drop of $j(m)$ triggers a GSF instability⁵. However, at the beginning of the interpulse period, the mixing and the consequent redistribution of $j(m)$ are inhibited by the steep gradient of mean molecular weight that separates the He-rich zone from the H-rich envelope. As a consequence, the internal border of the unstable zone remains almost fixed and close to the deepest point previously attained by the fully convective envelope at the time of the TDU. When the H burning restarts, a shallower μ gradient takes place and the GSF instability begins to move inward. At that time, the ^{13}C pocket is almost fully developed. As shown in Figure 2, such a zone partially overlaps with the ^{13}C pocket. As the interpulse goes on, the region affected by this instability grows in mass, due to the outward diffusion of the angular momentum: $j(m)$ decreases at the internal border, while it increases at the external one (see Figure 4). For this reason the upper border of the ^{13}C pocket is progressively dragged upward. Since the GSF instability is active in a ^{14}N -rich zone, it produces a contamination of the ^{13}C pocket with a strong neutron poison (see the second row in Figure 3). Also in this case, the larger v_{rot}^{ini} the higher v_{GSF} and the more extended the unstable zone (see Figure 2). Summarizing, in models with $v_{rot}^{ini} \leq 60$ km/s, the s-process nucleosynthesis is mainly affected by the GSF instability. On the contrary, meridional circulations provide an important additional modification of the ^{13}C pocket in fast rotating models.

The overall nucleosynthesis results of our calculations for the solar metallicity set are displayed in Figures 5 and 6, where we report the evolution of $[\text{ls}/\text{Fe}]$ ⁶, $[\text{hs}/\text{Fe}]$ ⁷ and of the $[\text{hs}/\text{ls}]$ index⁸ at the stellar surface. For $v_{rot}^{ini} \leq 60$ km/s, the larger the initial rotation velocity the smaller the final $[\text{ls}/\text{Fe}]$ and $[\text{hs}/\text{Fe}]$. This is a consequence of the ^{14}N contamination of the ^{13}C pocket

⁵This is the same GSF instability already found and discussed in previous works on rotating AGB models, (*e.g.* Herwig et al. 2003; Siess et al. 2004).

⁶ $[\text{ls}/\text{Fe}] = ([\text{Sr}/\text{Fe}] + [\text{Y}/\text{Fe}] + [\text{Zr}/\text{Fe}]) / 3$.

⁷ $[\text{hs}/\text{Fe}] = ([\text{Ba}/\text{Fe}] + [\text{La}/\text{Fe}] + [\text{Nd}/\text{Fe}] + [\text{Sm}/\text{Fe}]) / 4$.

⁸ $[\text{hs}/\text{ls}] = [\text{hs}/\text{Fe}] - [\text{ls}/\text{Fe}]$.

caused by the GSF instability. Moreover, the hs component is more depleted with respect to the ls component. The latter is a consequence of the lower neutrons-to-seeds ratio determined by the combined actions of the two secular rotation-induced instabilities previously described. Thus, the [hs/ls] spectroscopic index decreases when increasing v_{rot}^{ini} (see Figure 6). The model with $v_{rot}^{ini}=120$ km/s deviates from the described trend, as its [ls/Fe] and [hs/Fe] result larger than those of the models with $v_{rot}^{ini}=30$ km/s and $v_{rot}^{ini}=60$ km/s. Such an occurrence is due to the particularly efficient meridional circulations, which drives the formation of a more extended ^{13}C pocket. Note that, in any case, the [hs/ls] index decreases as v_{rot}^{ini} increases from 0 to 120 km/s.

3.3. TP-AGB evolution and the ^{13}C pocket: the [Fe/H]=-1.7 case

Low metallicity models exhibit the same global behavior, even if some important differences there exist. In general, we expect, and actually obtain as a result of our calculations, that the effects of rotation are stronger at low metallicity because stellar structures are more compact, so that for a given v_{rot}^{ini} the corresponding angular velocity is larger. Moreover, since at each TP some angular momentum is extracted from the He-intershell and since the first efficient TDU episode occurs earlier at low metallicity (Cristallo et al. 2009, and references therein), it comes out that at the first TDU episode, the angular velocity in the region where ^{13}C pocket will form is larger. As a consequence, the rotation-induced instabilities in low Z models are more efficient and affect at a higher level the s-process nucleosynthesis. In particular, the ES instability produces sizable effects even for low v_{rot}^{ini} . This occurrence is shown in Figure 7, where we report the same quantities as in Figure 2, but for the $1.5 M_{\odot}$ and [Fe/H]=-1.7 models.

The nucleosynthesis results are illustrated in Figure 8, where we report the evolution of the [ls/Fe], [hs/Fe] and [Pb/Fe] for all the computed models at [Fe/H]=-1.7. By increasing the initial rotation velocity, the [Pb/Fe] decreases more than one order of magnitude with respect to the non-rotating model, while [ls/Fe] and [hs/Fe] increase by a factor of 2 and 5, respectively. In low

metallicities non-rotating models, the high neutrons-to-seeds ratio favors the synthesis of a large amount of lead with respect to the hs and, to a larger extent, the ls components (see the discussion in Cristallo et al. 2009). Then, the strong lead suppression and the corresponding increase of ls and hs in rotating models are mainly due to the reduction of the neutrons-to-seeds ratio caused by both the GSF and the ES instabilities. For the same reason, the [hs/ls] decreases by a factor of ~ 3 while the [Pb/hs]⁹ decreases of more than a factor 20, reaching a value [Pb/hs] ~ 0 in the model with $v_{rot}^{ini}=120$ km/s (see Figure 9).

Note that, as for the solar Z models, the total amount of heavy elements is, in any case, smaller in rotating models. This is a consequence of the reduction of the total amount of neutrons available for the s process, as due to the ¹⁴N contamination of the ¹³C pocket induced by the GSF instability.

4. Uncertainties on the angular momentum transport and on the treatment of rotation-induced mixing

As already discussed in Section 2, the treatments of both the angular momentum transport and the rotation-induced mixing are affected by many uncertainties. In order to evaluate their effects on the final heavy elements s process surface distributions, we compute an additional set of models with $M=2 M_{\odot}$, $[Fe/H]=0$ and $v_{rot}^{ini}=30$ km/s, by adopting different values for the f_{μ} , f_c and f_{ω} parameters introduced in Equations (2), (5) and (9). Our results are summarized in Figure 10, where we report the [ls/Fe], [hs/Fe] and [hs/ls]. As a result, a general reduction of the efficiency of both the angular momentum transport and mixing of chemical species (model with $f_c=f_{\mu}=1$ and $f_{\omega}=0.1$: open circles with dotted lines) reduces the effect of rotation so that both the ls and

⁹[Pb/hs]=[Pb/Fe]-[hs/Fe] .

hs elements are overproduced with respect to the reference case ($f_c=f_\mu=f_\omega=1$: filled squares with solid lines). By recalling that at solar metallicity, for moderate values of the initial rotation velocity, the net effect of rotation-induced instabilities is a larger depletion of the hs component, it comes out that the model with $f_\omega=0.1$ attains a slightly higher [hs/l_s] (lower panel of Figure 10). The same conclusion is still valid for the model with $f_\mu=f_\omega=1$ and $f_c=0.04$ (open squares with long-dashed lines). Since the f_c parameter affects only the mixing of chemical species but not the transport of angular momentum, by comparing this model to the one with $f_c=f_\mu=1$ and $f_\omega=0.1$ we conclude that the s-process nucleosynthesis during the AGB phase is not significantly affected by the uncertainty related to the angular momentum transport. In this regard, it is important to note that for the model with $f_c=0.04$ the mixing efficiency of chemical species has been reduced by a factor larger than in the model with $f_\omega=0.1$. As a consequence, the corresponding [hs/Fe] results slightly larger, thus determining an increase of the [hs/l_s] index.

In order to test the sensitivity of the s process to the inhibiting effect of μ gradients on secular instabilities (ES and GSF), we compute a model with $f_c=f_\omega=1$ and $f_\mu=0.05$. Owing to the reduction of the μ -gradient barrier, the zones interested by both the GSF and the ES instabilities are larger and the effective circulation velocities increase. As a result, the final amount of l_s and hs elements is lower than what we find in the $f_\mu = 1$ case, but the final [hs/l_s] is only marginally modified (open squares with long dashed lines). It is important to remark that a decrease of f_μ is not equivalent to an increase of the efficiency of both angular momentum transport and mixing of chemical species (*e.g.* as obtained by increasing f_ω). In fact, on a general ground, the reduction of μ -currents determines not only the increase of the efficiency of rotation-induced instabilities, but also the enlargement of the unstable zones.

Finally, we have computed two additional models by fixing $f_\omega = 1$, $f_\mu = 0.05$ and $f_c = 0.04$ for two different values of the initial rotation velocity, namely $v_{rot}^{ini} = 30$ km/s and $v_{rot}^{ini} = 60$ km/s. The obtained results are displayed in Figure 11, where we report the evolution of the surface [l_s/Fe], [hs/Fe] and [hs/l_s]. For comparison we also plot the same quantities for models with

$f_c = f_\mu = f_\omega = 1$ and $v_{rot}^{ini} = 10$ km/s (filled triangles with solid line), $v_{rot}^{ini} = 30$ km/s (filled squares with solid line) and $v_{rot}^{ini} = 60$ km/s (filled circles with solid line). By an inspection to Figure 11 it comes out that models with reduced f_c and f_μ mimic models with lower initial rotation velocities and $f_c = f_\mu = 1$. As a matter of fact, the overall uncertainties produced by varying the three free parameters do not exceed the variations of the surface chemical abundances obtained by changing the initial rotation velocity within the range explored in this paper.

Finally, we have computed a few additional models in order to reproduce the mean-core-rotation period (20-200 days) derived by Mosser et al. (2012) for a sample of red clump stars with solar-like metallicity. We found that the efficiency of angular momentum transport should be increased by a factor of at least 1000. In practice, we are able to reproduce the asteroseismic data by setting $f_\omega > 1000$ and, accordingly, by reducing f_c in order to maintain $f_\omega \cdot f_c = 1$. In this way, with respect to our standard model ($f_\omega = f_c = 1$), the mean angular velocity in the He-core decreases by roughly a factor 200 down to 1.4×10^{-6} rad/s. In such a model, at the onset of the TP-AGB phase the angular velocity in the He-intershell is also two orders of magnitude smaller than in the standard case. Thus, the ES and GSF induced mixing marginally modifies the mass extensions of the ^{13}C and ^{14}N pockets and their relative overlap. As a consequence, the resulting s-process surface enrichment is very similar to the non-rotating model. We will further comment this result in the next Section.

5. Summary and Conclusions

We investigated the effects of rotation on the s-process nucleosynthesis in low-mass AGB stars by computing full evolutionary models from the pre-Main Sequence up to the AGB tip. In our computations we included the angular momentum transport and the mixing of chemical species, as determined by convection and rotation-induced instabilities. We also discussed the uncertainties affecting the efficiencies of angular momentum transport and mixing.

In Table 2, we report the final values of [ls/Fe], [hs/Fe], [Pb/Fe], [hs/ls] and [Pb/hs] for all the computed models. The evolution of the abundances of elements and isotopes as well as the chemical yields related to the models presented in this paper will be available on the FRUITY database¹⁰ (Cristallo et al. 2011). In the same Table we also report the final carbon surface enhancements for the computed models, assumed as representative of the mass globally dredged up during the AGB phase. It is worth mentioning that the inclusion of rotation does not substantially alter the surface [C/Fe], thus confirming that its effects on the TDU efficiency are minimal. The largest differences characterizing models with $v_{rot}^{ini}=120$ km/s can be safely attributed to the larger core masses at the beginning of the AGB phase (see Straniero et al. 2003 for a detailed description of the relation between core mass and TDU efficiency).

Our analysis shows that a variation in the initial velocity determines a consistent spread in the final surface s-process enhancements and spectroscopic indexes in stars with the same initial mass and metallicity. Rotation-induced instabilities modify the mass extension of both the ¹³C and the ¹⁴N pockets and their overlap. The average neutrons-to-seeds ratio is also reduced. This has two major consequences: i) the total amount of heavy elements produced by the s process is lower and ii) the surface abundances are redistributed in such a way to favor the light-s elements with respect to the heavier ones. As a matter of fact, both the [hs/ls] and the [Pb/hs] spectroscopic indexes decrease as the initial rotation velocity increases. Our results suggest that rotation can be regarded as a possible physical mechanism responsible for the observed spread of the [hs/ls] index. Particularly interesting is the strong reduction of [Pb/hs] in rotating models. In this regard, we recall that the origin of lead in the solar system is usually ascribed to low metallicity AGB stars. Theoretical models show that the maximum lead production occurs at $Z \sim 10^{-3}$. Rare are lead measurements in low metallicity AGB and post-AGB stars belonging to the Galactic disk. On the other hand, a direct observation of Halo AGB stars presently undergoing TDU is not possible

¹⁰Available at fruity.oa-teramo.inaf.it.

as they have already evolved to their cooling sequence. However, the imprint of this ancient stellar population can be detected in Carbon-Enhanced-Metal-Poor stars enriched in s elements. Most of these stars are heavily enriched in Pb, even if some of them show a relatively low [Pb/hs] (see Bisterzo et al. 2011). Also in this case rotation can be regarded as a possible explanation of the observed spread in the heavy elements distributions.

The obtained results depend on the efficiency of angular momentum transport during the pre-AGB evolution. In particular, if the inner zones of a rotating star are efficiently spun down, as suggested by a recent analysis of rotational splittings in a sample of RGB and red clump stars with solar-like metallicity observed by Kepler, the rotation induced instabilities during the TP-AGB phase do not significantly alter the s-process nucleosynthesis. Note, however, that these observations are still rather limited in mass and chemical composition. In particular, we do not know if such a spin down of the core is so efficient also at the metallicity of Halo stars. Further observational constraints on the efficiency of angular momentum transport in low- and intermediate-mass stars can be derived from the rotational broadening of the Ca II K line in WDs (Berger et al. 2005). Rotation velocities up to 10 km/s, with an average value of about 1 km/s, have been observed. By adopting the same procedure described by Suijs et al. (2008) to derive the WDs rotation velocity from the last computed model at the tip of the AGB, we find that our standard model with $M=2 M_{\odot}$, $[Fe/H]=0$ and $v_{rot}^{ini}=30$ km/s produces a WD of $M= 0.63 M_{\odot}$ with $v_{rot}^{WD} = 58$ km/s. The same model, but with $f_{\omega} > 1000$ (see §4), leads to $v_{rot}^{WD} < 0.3$ km/s. Therefore, if models preserving the core angular momentum predict too short WDs rotation periods, those in which the core is substantially spun down, as required by asteroseismic observations of red clump stars, predict rather long WDs rotation periods.

We thank the anonymous referee for a careful and constructive reading of the manuscript. We acknowledge support from the Italian Ministry of Education, University and Research under the FIRB2008 program (RBFR08549F-002) and from the PRIN-INAF 2011 project "Multiple

populations in Globular Clusters: their role in the Galaxy assembly”.

REFERENCES

- Abia, C., Busso, M., Gallino, R., et al. 2001, *Astroph. J.*, 559, 1117
- Abia, C., Domínguez, I., Gallino, R., et al. 2002, *Astroph. J.*, 579, 817
- Ammeler-von Eiff, M. & Reiners, A. 2012, *Astron. Astroph.*, 542, A116
- Becker, S. A. & Iben, Jr., I. 1980, *Astroph. J.*, 237, 111
- Berger, L., Koester, D., Napiwotzki, R., Reid, I. N., & Zuckerman, B. 2005, *Astron. Astroph.*, 444, 565
- Bisterzo, S., Gallino, R., Straniero, O., Cristallo, S., & Käppeler, F. 2011, *MNRAS*, 418, 284
- Brott, I., de Mink, S. E., Cantiello, M., et al. 2011, *Astron. Astroph.*, 530, A115
- Castellani, V., Chieffi, A., & Straniero, O. 1990, *Astroph. J. Suppl.*, 74, 463
- Chaboyer, B. & Zahn, J.-P. 1992, *Astron. Astroph.*, 253, 173
- Chieffi, A. & Limongi, M. 2013, *Astroph. J.*, 764, 21
- Cox, J. P. 1968, *Principles of stellar structure - Vol.1: Physical principles; Vol.2: Applications to stars*
- Cristallo, S., Piersanti, L., Straniero, O., et al. 2011, *Astroph. J. Suppl.*, 197, 17
- Cristallo, S., Straniero, O., Gallino, R., et al. 2009, *Astroph. J.*, 696, 797
- de Medeiros, J. R. & Mayor, M. 1999, *A&AS*, 139, 433
- Denissenkov, P. A. & Pinsonneault, M. 2007, *Astroph. J.*, 655, 1157
- Denissenkov, P. A. & Tout, C. A. 2003, *MNRAS*, 340, 722

- Dominguez, I., Straniero, O., Tornambe, A., & Isern, J. 1996, *Astroph. J.*, 472, 783
- Eggenberger, P., Montalbán, J., & Miglio, A. 2012, *Astron. Astroph.*, 544, L4
- Endal, A. S. & Sofia, S. 1976, *Astroph. J.*, 210, 184
- Endal, A. S. & Sofia, S. 1978, *Astroph. J.*, 220, 279
- Fricke, K. 1968, *ZAp*, 68, 317
- Gallino, R., Arlandini, C., Busso, M., et al. 1998, *Astroph. J.*, 497, 388
- Goldreich, P. & Schubert, G. 1967, *Astroph. J.*, 150, 571
- Gough, D. O. & McIntyre, M. E. 1998, *Nature*, 394, 755
- Groot, P. J., Pitters, A. J. M., & van Paradijs, J. 1996, *A&AS*, 118, 545
- Heger, A., Langer, N., & Woosley, S. E. 2000, *Astroph. J.*, 528, 368
- Heger, A., Woosley, S. E., & Spruit, H. C. 2005, *Astroph. J.*, 626, 350
- Herwig, F., Bloeker, T., Schoenberner, D., & El Eid, M. 1997, *Astron. Astroph.*, 324, L81
- Herwig, F., Langer, N., & Lugaro, M. 2003, *Astroph. J.*, 593, 1056
- Holmberg, J., Nordström, B., & Andersen, J. 2007, *Astron. Astroph.*, 475, 519
- Iben, Jr., I. & Renzini, A. 1983, *ARA&A*, 21, 271
- James, R. A. & Kahn, F. D. 1971, *Astron. Astroph.*, 12, 332
- Kawaler, S. D. 1988, *Astroph. J.*, 333, 236
- Kippenhahn, R. 1974, in *IAU Symposium, Vol. 66, Late Stages of Stellar Evolution*, ed. R. J. Tayler & J. E. Hesser, 20

- Kippenhahn, R. & Thomas, H.-C. 1970, in IAU Colloq. 4: Stellar Rotation, ed. A. Slettebak, 20
- Lambert, D. L., Smith, V. V., Busso, M., Gallino, R., & Straniero, O. 1995, *Astroph. J.*, 450, 302
- Langer, N. 2012, *ARA&A*, 50, 107
- Langer, N., Heger, A., Wellstein, S., & Herwig, F. 1999, *Astron. Astroph.*, 346, L37
- Lodders, K. 2003, *Astroph. J.*, 591, 1220
- Marques, J. P., Goupil, M. J., Lebreton, Y., et al. 2013, *Astron. Astroph.*, 549, A74
- Mosser, B., Goupil, M. J., Belkacem, K., et al. 2012, *Astron. Astroph.*, 548, A10
- Mowlavi, N. 1999, *Astron. Astroph.*, 344, 617
- Petrovic, J., Langer, N., Yoon, S.-C., & Heger, A. 2005, *Astron. Astroph.*, 435, 247
- Piersanti, L., Cabezón, R. M., Zamora, O., et al. 2010, *Astron. Astroph.*, 522, A80
- Piersanti, L., Gagliardi, S., Iben, Jr., I., & Tornambé, A. 2003, *Astroph. J.*, 583, 885
- Piersanti, L., Straniero, O., & Cristallo, S. 2007, *Astron. Astroph.*, 462, 1051
- Pinsonneault, M. H., Kawaler, S. D., Sofia, S., & Demarque, P. 1989, *Astroph. J.*, 338, 424
- Przybilla, N., Firnstein, M., Nieva, M. F., Meynet, G., & Maeder, A. 2010, *Astron. Astroph.*, 517, A38
- Reimers, D. 1975, *Circumstellar envelopes and mass loss of red giant stars*, ed. B. Baschek, W. H. Kegel, & G. Traving, 229–256
- Reyniers, M., Van Winckel, H., Gallino, R., & Straniero, O. 2004, *Astron. Astroph.*, 417, 269
- Siess, L., Goriely, S., & Langer, N. 2004, *Astron. Astroph.*, 415, 1089

Spruit, H. C. 1998, *Astron. Astroph.*, 333, 603

Spruit, H. C. 2002, *Astron. Astroph.*, 381, 923

Straniero, O., Domínguez, I., Cristallo, S., & Gallino, R. 2003, *PASA*, 20, 389

Straniero, O., Gallino, R., Busso, M., et al. 1995, *Astroph. J. Lett.*, 440, L85

Straniero, O., Gallino, R., & Cristallo, S. 2006, *Nuclear Physics A*, 777, 311

Suijs, M. P. L., Langer, N., Poelarends, A.-J., et al. 2008, *Astron. Astroph.*, 481, L87

Tornambé, A. & Piersanti, L. 2013, *MNRAS*

Yoon, S.-C. & Langer, N. 2004, *Astron. Astroph.*, 419, 623

Yoon, S.-C. & Langer, N. 2005, *Astron. Astroph.*, 443, 643

Yoon, S.-C., Langer, N., & Norman, C. 2006, *Astron. Astroph.*, 460, 199

Zahn, J.-P., Talon, S., & Matias, J. 1997, *Astron. Astroph.*, 322, 320

Table 1. Physical properties of the computed models (see text for details).

[Fe/H]	M	v_{rot}^{ini}	ω_0	J_0	τ_{MS}	M_H^{TIP}	$\tau_{He-burn}$	t_{AGB}	M_{CO}^{AGB}	M_H^{AGB}	C/O
	[M_\odot]	[km/s]	[$10^{-4} rad/s$]	[$10^{50} g cm^2/s$]	[$10^8 yr$]	[M_\odot]	[$10^8 yr$]	[$10^8 yr$]	[M_\odot]	[M_\odot]	
0	2.0	0	0.00	0.00	9.693	0.4628	1.212	12.240	0.512	0.545	0.253
0	2.0	10	0.09	0.22	9.702	0.4651	1.196	12.248	0.513	0.545	0.255
0	2.0	30	0.28	0.65	9.706	0.4653	1.194	12.256	0.517	0.550	0.257
0	2.0	60	0.56	1.30	9.714	0.4659	1.190	12.279	0.519	0.550	0.257
0	2.0	120	1.09	2.61	9.783	0.4686	1.147	12.385	0.532	0.561	0.267
-1.7	1.5	0	0.00	0.00	16.470	0.4794	0.913	19.973	0.548	0.579	0.394
-1.7	1.5	10	0.14	0.14	16.468	0.4795	0.913	19.970	0.545	0.574	0.395
-1.7	1.5	30	0.42	0.43	16.493	0.4797	0.908	19.984	0.548	0.577	0.399
-1.7	1.5	60	0.84	0.86	16.542	0.4799	0.900	20.050	0.552	0.581	0.404
-1.7	1.5	120	1.70	1.70	16.905	0.4811	0.885	20.474	0.561	0.587	0.406

Table 2. Surface s-process enhancements, s-process indexes and [C/Fe] for all the computed models.

[Fe/H]	M (M _⊙)	v_{rot}^{ini} (km/s)	[ls/Fe]	[hs/Fe]	[Pb/Fe]	[hs/ls]	[Pb/hs]	[C/Fe]
0	2.0	0	1.02	0.80	0.50	-0.22	-0.30	0.52
0	2.0	10	0.96	0.65	0.35	-0.31	-0.30	0.51
0	2.0	30	0.80	0.39	0.13	-0.41	-0.26	0.51
0	2.0	60	0.70	0.23	0.05	-0.47	-0.18	0.51
0	2.0	120	0.90	0.42	0.06	-0.48	-0.36	0.46
-1.7	1.5	0	0.89	1.39	2.79	0.50	1.40	2.31
-1.7	1.5	10	0.97	1.41	2.66	0.44	1.26	2.28
-1.7	1.5	30	1.09	1.46	2.39	0.37	0.93	2.28
-1.7	1.5	60	1.37	1.63	2.09	0.26	0.47	2.26
-1.7	1.5	120	1.57	1.62	1.62	0.04	0.01	2.20

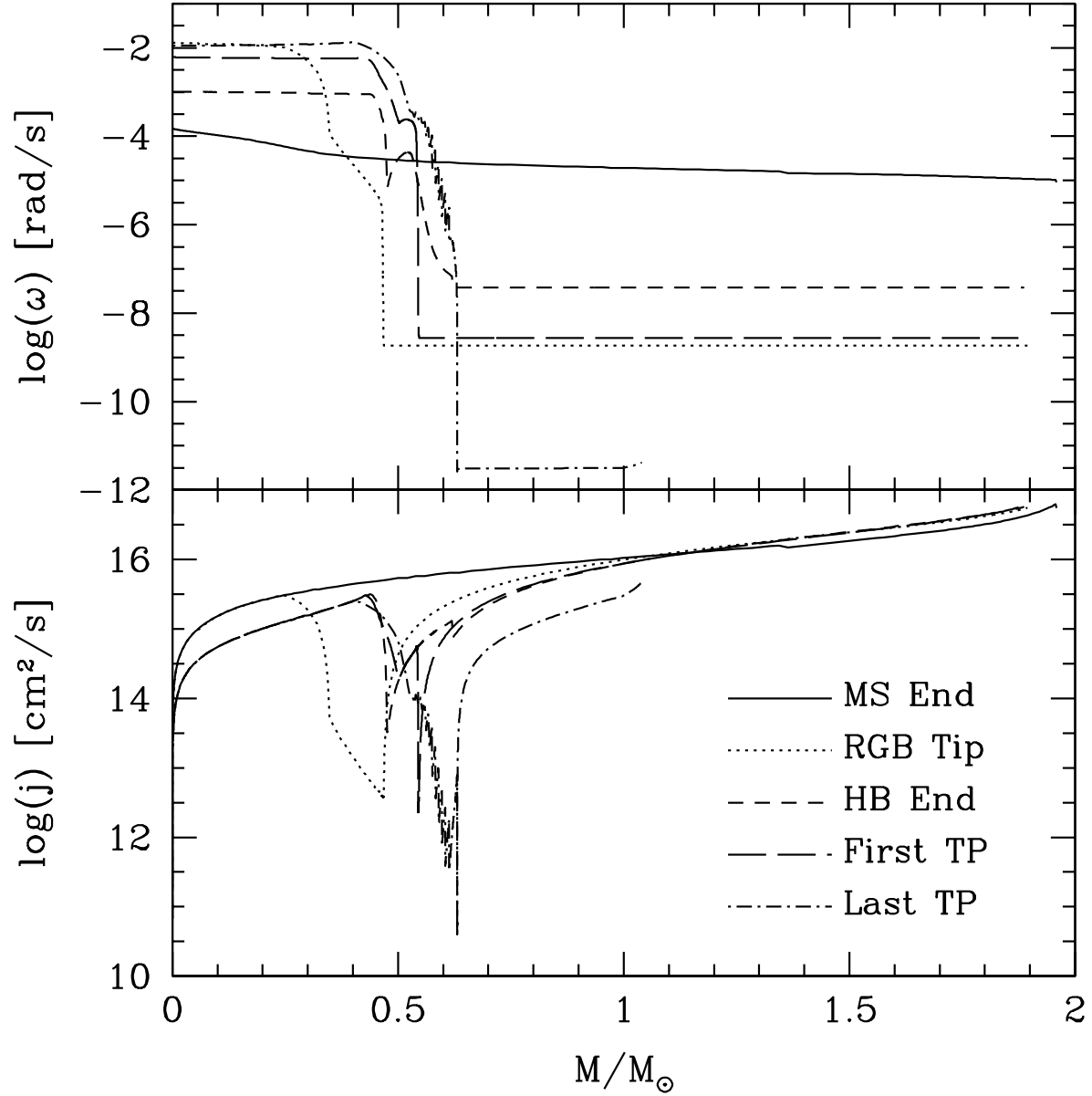


Fig. 1.— Evolution of angular velocity (upper panel) and specific angular momentum (lower panel) for the model with $M=2 M_{\odot}$, $[\text{Fe}/\text{H}]=0$ and $v_{rot}^{ini} = 30 \text{ km/s}$. Each curve refers to a different epoch (see text for details).

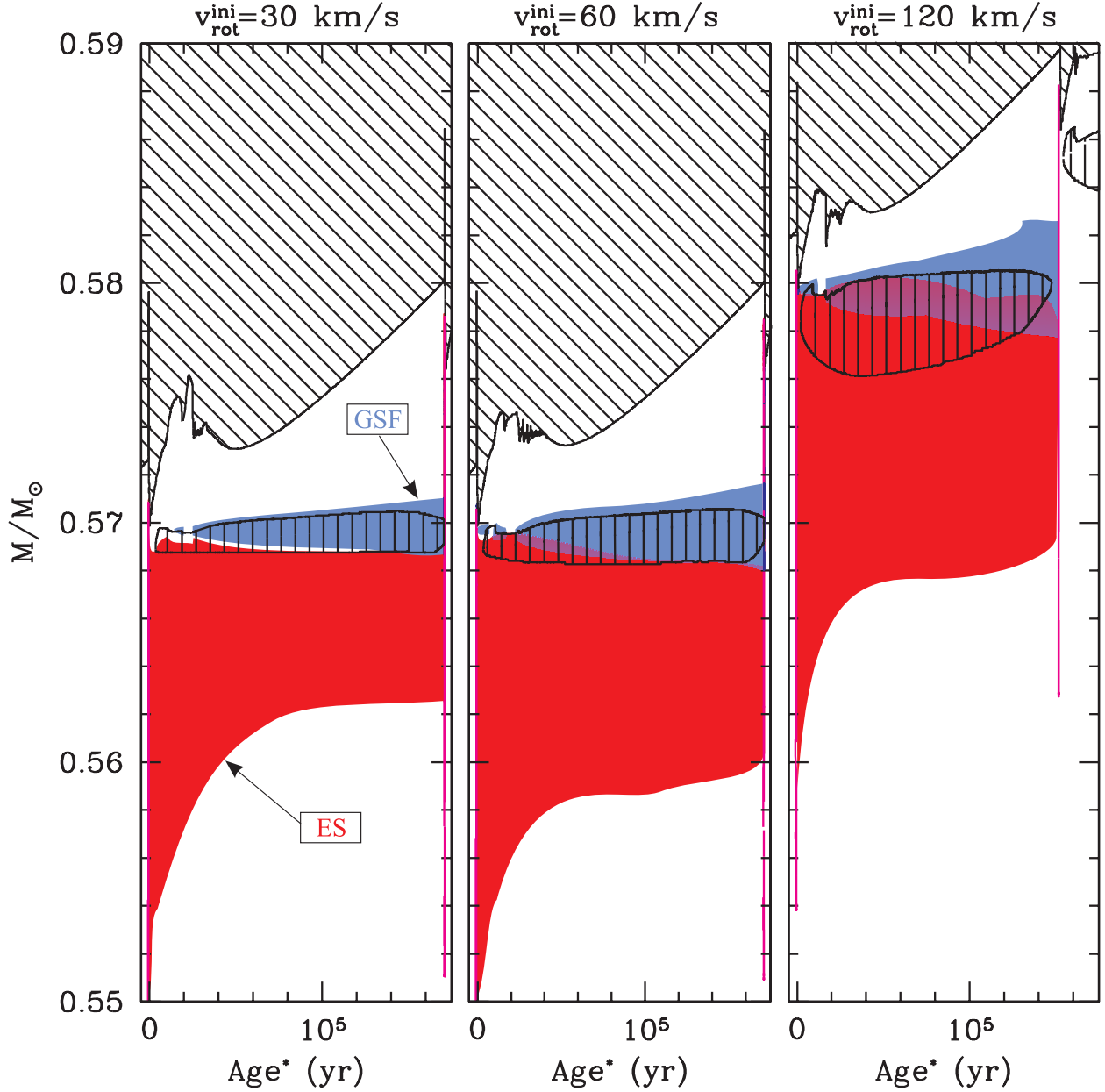


Fig. 2.— Temporal evolution of rotation-induced instabilities relevant for the s-process nucleosynthesis during the interpulse period between the 2nd and the 3rd TPs of the 2 M_{\odot} model with $[Fe/H]=0$ and different v_{rot}^{ini} . $t=0$ on the x-axis scale coincides with the epoch of the maximum convective envelope penetration during the 2nd TDU episode. Blue areas identify Goldreich-Schubert-Fricke unstable regions; red areas identify Eddington-Sweet unstable regions. Magenta spikes mark the convective shells powered by TPs. The oblique shaded area highlights the convective envelope, while the vertical shaded area is the region occupied by the ^{13}C -pocket.

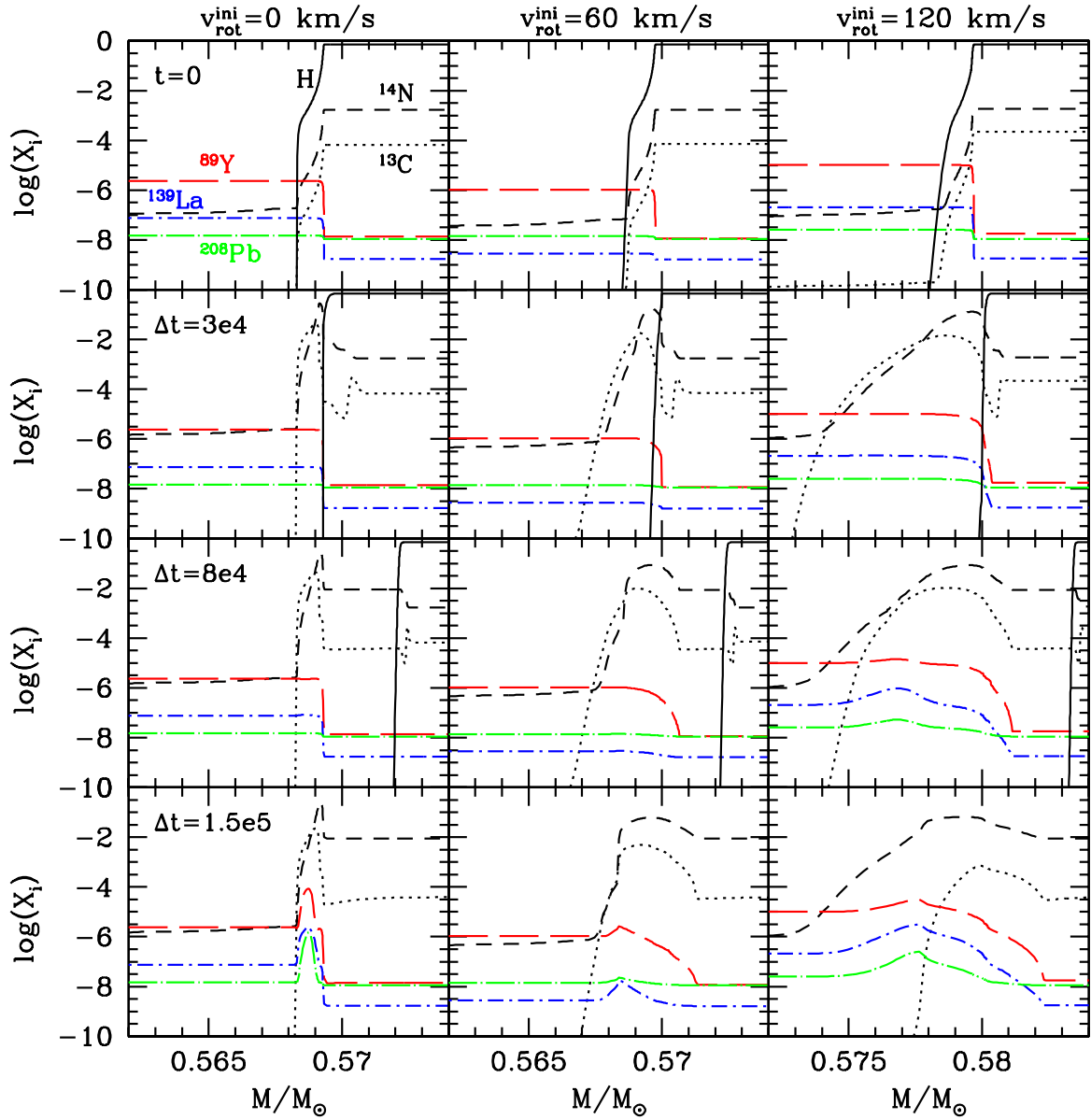


Fig. 3.— Evolution of key selected isotopes in the region where the ^{13}C pocket forms during the interpulse after the 2nd TDU for the $M=2 M_{\odot}$, $[\text{Fe}/\text{H}]=0$ model with different initial rotation velocities: H (solid), ^{13}C (dotted), ^{14}N (short-dashed), ^{89}Y (long-dashed), ^{139}La (dot-short-dashed) and ^{208}Pb (dot-long-dashed) (see the on-line edition for a color version).

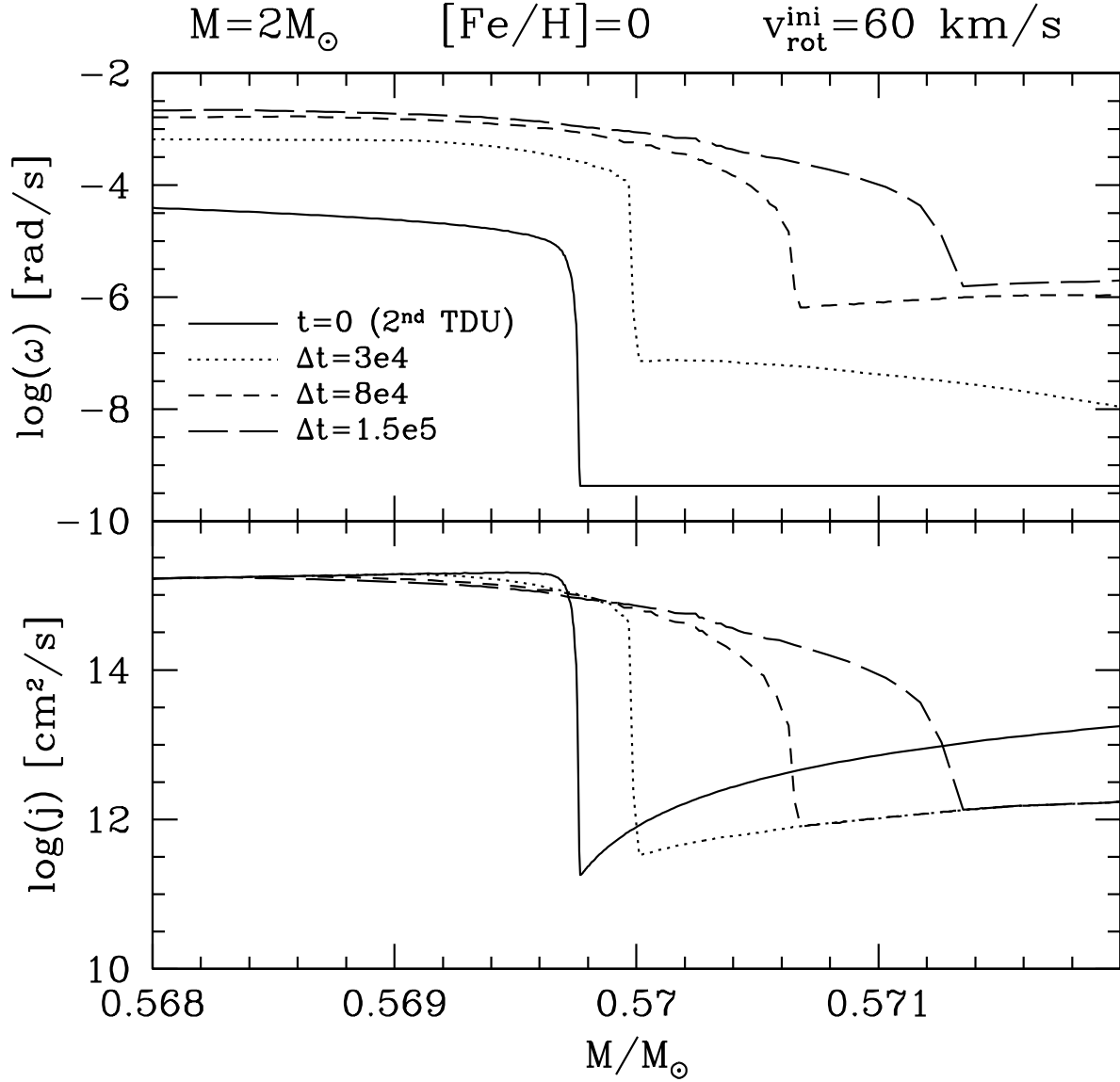


Fig. 4.— Angular velocity (upper panel) and specific angular momentum (lower panel) in the region interested by the 2nd TDU for the $M=2 M_{\odot}$, $[Fe/H]=0$ model with $v_{rot}^{ini} = 60$ km/s. The various curves refer to different epochs (see text for details).

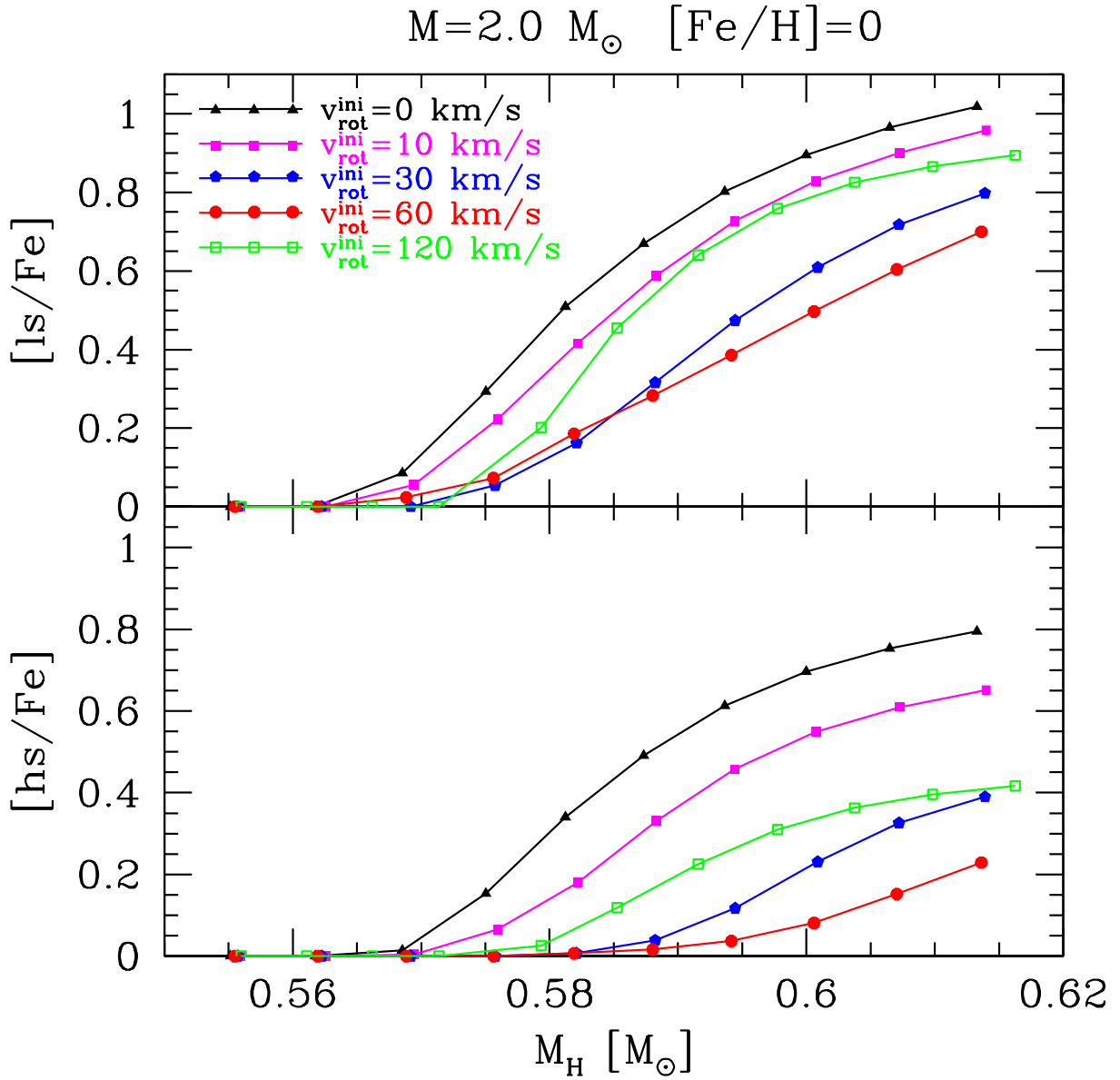


Fig. 5.— Evolution of $[\text{ls}/\text{Fe}]$ and $[\text{hs}/\text{Fe}]$ as a function of the core mass for the $2.0 M_{\odot}$ model with $[\text{Fe}/\text{H}]=0$. Each curve refers to a different initial rotation velocity (see the on-line edition for a color version).

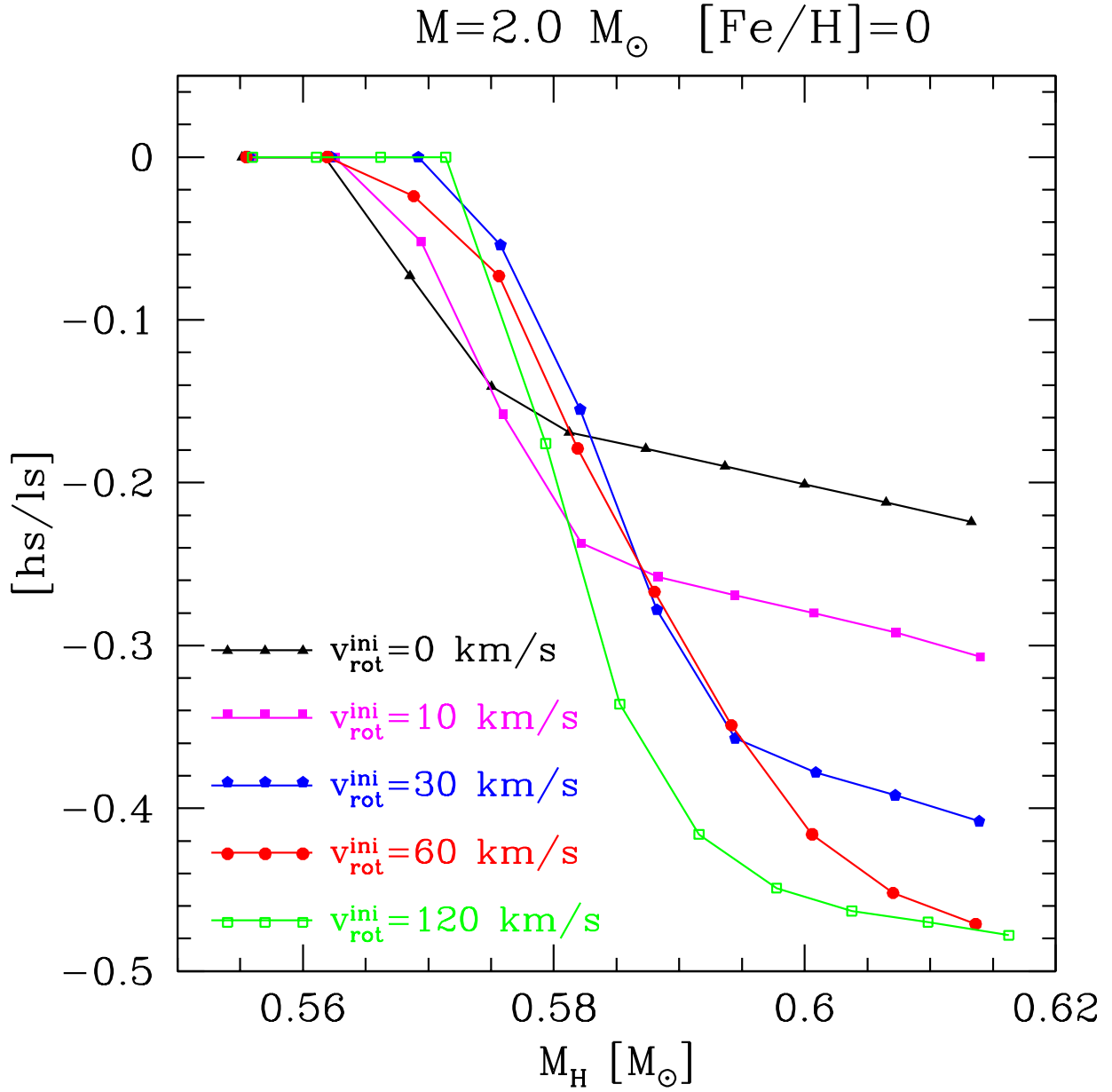


Fig. 6.— The same as in Figure 5, but for the $[\text{hs}/\text{ls}]$ spectroscopic index (see the on-line edition for a color version of this figure).

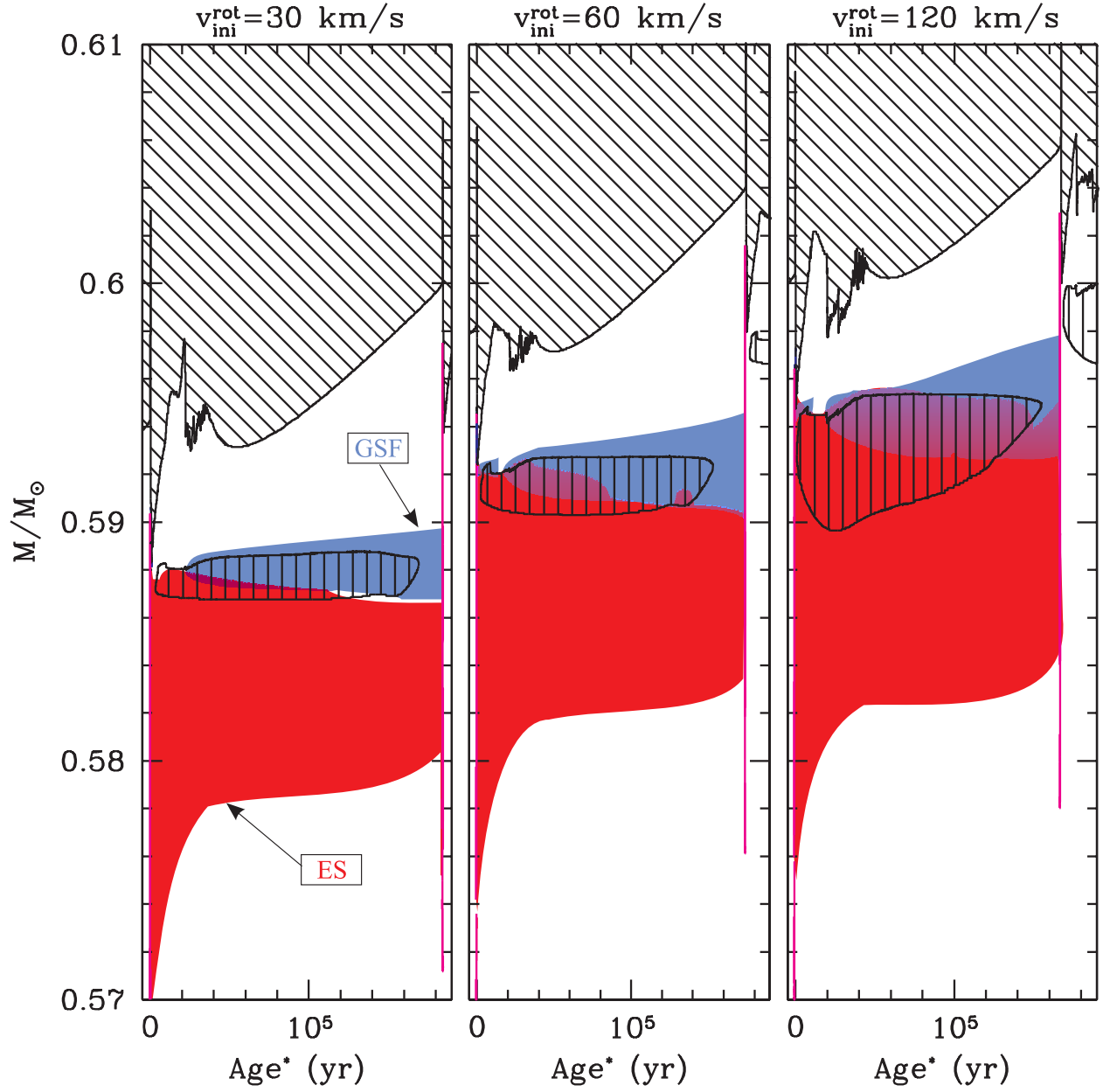


Fig. 7.— The same as in Figure 2, but for the $1.5 M_{\odot}$ model with $[\text{Fe}/\text{H}]=-1.7$.

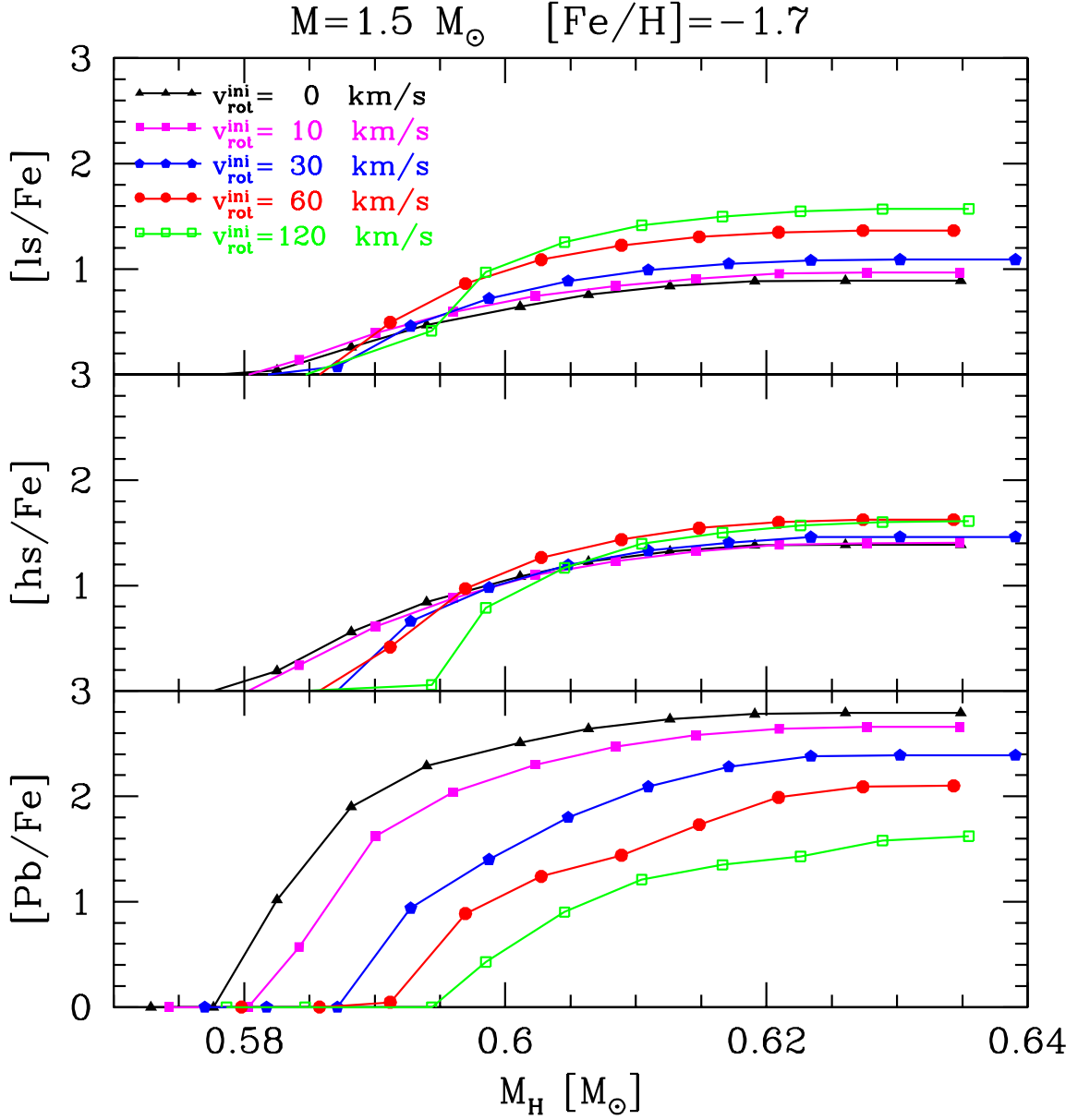


Fig. 8.— Evolution of of $[\text{ls}/\text{Fe}]$, $[\text{hs}/\text{Fe}]$ and $[\text{Pb}/\text{Fe}]$ as a function of the core mass for the $1.5 M_{\odot}$ model with $[\text{Fe}/\text{H}] = -1.7$. Each curve refers to a different initial rotation velocity (see the on-line edition for a color version).

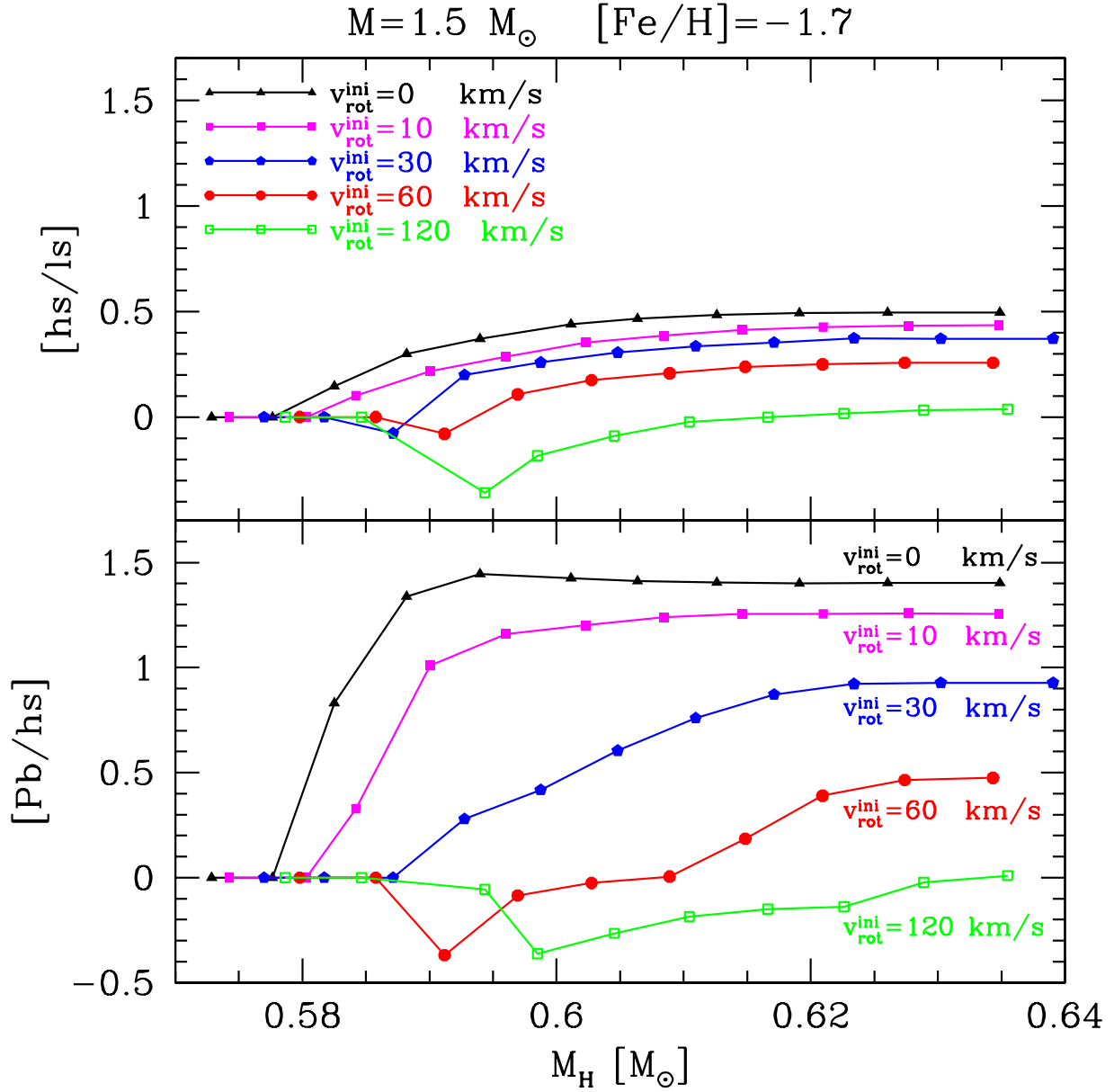


Fig. 9.— The same as in Figure 8, but for the [hs/ls] and [Pb/hs] spectroscopic indexes (see the on-line edition for a color version).

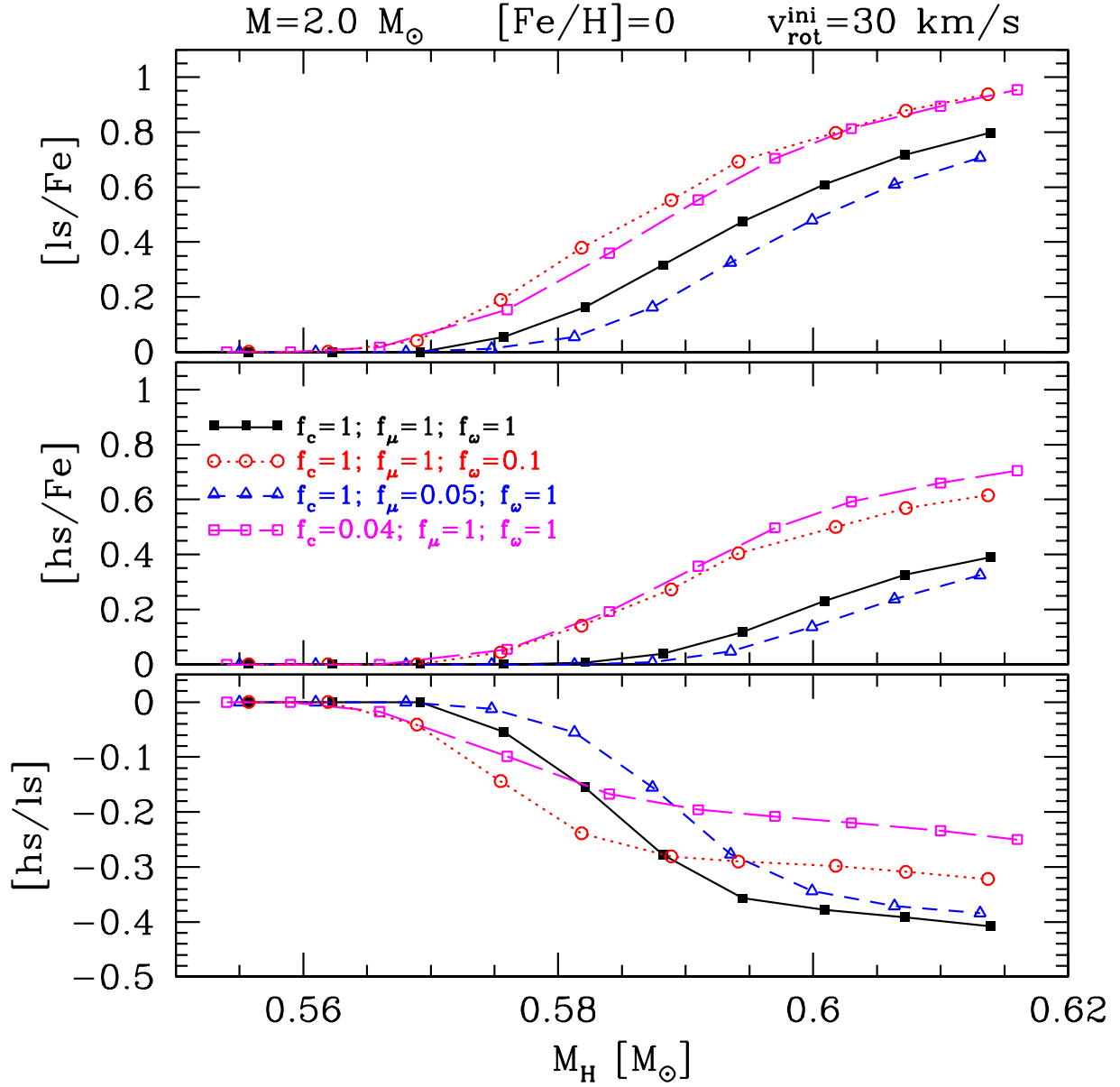


Fig. 10.— Evolution of $[\text{ls}/\text{Fe}]$, $[\text{hs}/\text{Fe}]$ and $[\text{hs}/\text{ls}]$ for the $2.0 M_{\odot}$ model with $[\text{Fe}/\text{H}]=0$ and $v_{\text{rot}}^{\text{ini}}=30$ km/s, with different choices for the free parameters (see the on-line edition for a color version).

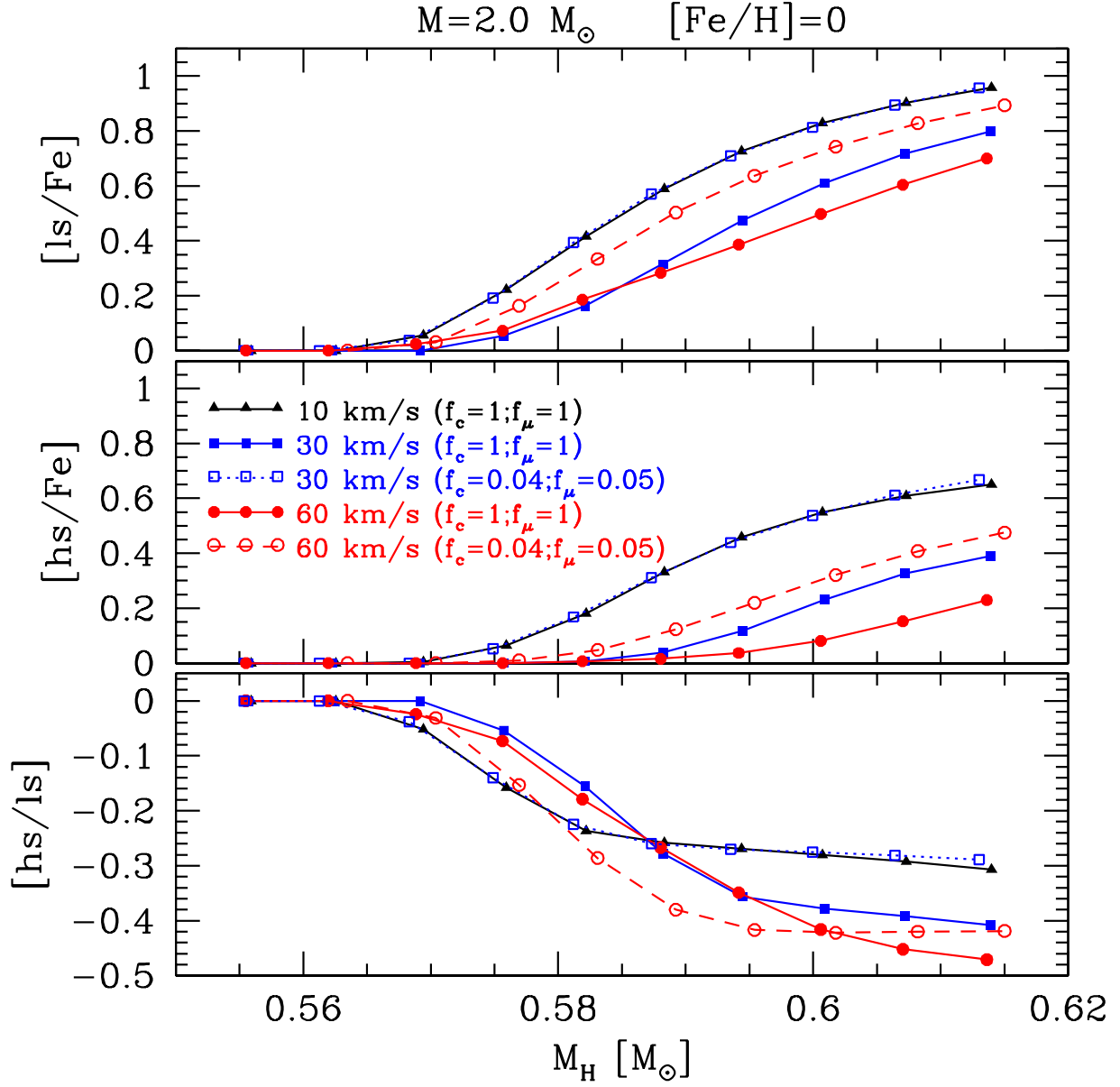


Fig. 11.— The same as in Figure 11, but for different initial rotation velocities and free parameters combinations (see the on-line edition for a color version).